The Formation of Clusters and Large-Scale Structures: Panoramic View of the High-z Universe with Subaru Telescope

M. Ouchi
Hubble Fellow / STScI, Baltimore, MD 21218, USA
SXDS team

We present early results from our on-going survey for proto-clusters and large-scale structures at $z = 3-6$. We carried out very deep wide-field optical imaging down to $i' = 27.5$ for the 1 deg^2 field of the Subaru/XMM-Newton Deep Field with 8.2m Subaru Telescope. We obtained maps of the Universe traced by $\sim 20,000$ Lyman break galaxies at $z = 3.5-6.2$ and by $\sim 1,000$ Ly-a galaxies at $z = 3.1$, 3.7, and 5.7. These cosmic maps have a transverse dimension of $\sim$ 150 Mpc $\times$150 Mpc in comoving units at each redshift, and provide us, for the first time, a panoramic view of these early Universe from the scales of galaxies, clusters to large-scale structures with a large number of high-z galaxies. For scales of galaxies, we show the definitive detection of small-scale excess of angular correlation functions for LBGs. The combination of the small- and large-scale bias indicates that multiple high-z galaxies occupy a single dark halo with an average mass of $10^{11}-10^{12}M_{\odot}$. For scales of clusters to large-scale structures, we report the discovery of filamentary large-scale structures (LSSs) made of LAEs at $z = 5.7$. In the densest regions of the filamentary LSSs at $z = 5.7$, we found two concentrations of LAEs at $z = 5.67$ and 5.69. These concentrations show about 130 times higher star-formation rate density than the mean field. These concentrations would be clusters in a formation phase involving a burst of galaxy formation.

1. Introduction

Recently, there has been a great progress in observational studies of structures of the high-redshift Universe. Based on statistical analyses, strong clustering signals are detected in the angular correlation functions (ACFs) of Lyman break galaxies (LBGs; e.g. [1–3]) at $z = 3-5$ and Ly α emitters (LAEs; [4, 5]) at $z \simeq 5$. These clustering results indicate that distribution of high-z galaxies is fairly inhomogeneous and highly biased against matter distribution predicted by the hierarchical model, i.e., the Cold Dark Matter (CDM) model (e.g. [6]). These biased distribution of high-z galaxies are well understood with the inhomogeneous distribution of dark halos and bias of galaxy formation (e.g. [7]). However, we have little knowledge about the relation between high-z galaxies and dark halos because of the small statistics.

On the other hand, various structures of high-z galaxies have been identified. A proto-cluster at $z = 3.1$ with a large population of LBGs were discovered by [8]. A significant excess of LAEs was found by [9] around a radio galaxy at $z = 4.1$, and a subsequent study concluded that this excess is indeed a proto-cluster with a size of $3-5$ Mpc [10]. More recently, clustering of 6 LAEs near a radio galaxy at $z \sim 5.2$ was reported [11]. For structures beyond cluster scales, wide-field narrow-band surveys revealed very inhomogeneous distribution of LAEs [4, 5, 12–14] at $z \simeq 5-6$. [12] report an elongated overdense region of LAEs at $z = 4.86$ on the sky of 20 Mpc in width and 50 Mpc in length. However, on the same sky, there was no large-scale structure at $z = 4.79$ which is closer to us by 39 Mpc, indicating a large cosmic variance over their surveyed volumes [5]. Although a few segments of high-z structures have been found to date, the whole picture of high-z Universe is veiled. Moreover, we do not know when and how the structures of galaxies seen at present formed from the initial matter density fluctuations. We started a systematic survey to map the high-z Universe with LBGs and LAEs at $3 < z < 7$ in the 1 deg^2 sky of the Subaru/XMM-Newton Deep Field (SXDF: R.A.$= 2^h18^m00^s$, decl.$= -5°00'00''$[J2000]; [15]). We obtain cosmic maps on scales of much larger than present-day LSSs to cover a network of LSSs at several redshifts between $z = 3$ and 7. In this contribution, we report the initial results of our survey about structures made of high-z galaxies at $z = 3-6$. Throughout this contribution, we present magnitudes in the AB system and adopt $H_0 = 70h_{70}$km s^{-1} Mpc^{-1} and $[\Omega_m, \Omega_\Lambda, n, \sigma_8] = [0.3, 0.7, 1.0, 0.9]$.

2. Data and Samples

We carried out deep optical broad-band and narrow-band imaging with Subaru/Suprime-Cam [16] in the 1 deg^2 sky of the SXDF. Our broad-band (B, V, R, i', and z') images reach $B \simeq 28.3$, $V \simeq 27.3$, $R \simeq 27.6$, $i' \simeq 27.5$, and $z' \simeq 26.5$ with a $2''$-diameter circular aperture at the 3σ level (Furusawa et al. in prep.; see [15]). We obtained narrow-band images with three bands, $NB503$ ($\lambda_c = 5030$Å, $\Delta\lambda = 70$Å) , $NB570$ ($\lambda_c = 5700$Å, $\Delta\lambda = 70$Å), and $NB816$ ($\lambda_c = 8150$Å, $\Delta\lambda = 120$Å). The 5σ sky noise of these narrow-band images are $NB503 \simeq 25.2$, $NB570 \simeq 25.0$, and $NB816 \simeq 26.0$ in a $2''$-diameter circular aperture (see [17] for the $NB816$ data). These narrow-band filters enable us to identify LAEs, galaxies with a strong Lyα emission line, at $z \simeq 3.1 \pm 0.03$, 3.7 ± 0.03, and 5.7 ± 0.05 with a small fraction of fore-

Table I High-z Galaxy Samples in the SXDF

Sample Name	Redshift	Number	Magnitude Limit
BRi-LBG	4.0 ± 0.5	16,920	$i' < 27.5$
Viz-LBG	4.7 ± 0.5	2,768	$z' < 26.5$
Riz-LBG	4.9 ± 0.3	1,293	$z' < 26.5$
i-dropout	5.9 ± 0.3	133	$z' < 26.0$
$NB503$-LAE	3.1 ± 0.03	332	$NB503 < 25.2$
$NB570$-LAE	3.7 ± 0.03	175	$NB570 < 25.0$
$NB816$-LAE	5.7 ± 0.05	515	$NB816 < 26.0$

ground contaminants (20-30%; [12, 14, 18]). Typical seeing sizes of these images are $\sim 0''.8$. The data were reduced with a software package SDFRED [19, 20].

We carry out object detection and photometry with SExtractor [21]. We detect 0.6 million objects with $i' < 27.5$, and measure colors for these objects. We make 5 catalogs each of which is based on i', z', $NB503$, $NB570$, and $NB816$-band detection. We select LBGs based on the 3 sets of color-color diagram, $(B-R, R-i')$, $(V-i', i'-z')$, and $(R-i', i'-z')$. We refer LBGs selected with these color-color diagrams to BRi-LBGs, Viz-LBGs, and Riz-LBGs, respectively. Our i-dropouts are selected with a single color of $i'-z'$ and constraints for the non-detection of blue continuum in B, V, and R bands. We isolate LAEs with their narrow-band excess colors as well as with a continuum color if the broad-band photometry bluer than the narrow-band is available.

We define the color criteria for LBGs, i-dropouts, and LAEs as

$$B-R > 1.2,\ R-i' < 0.7,\ B-R > 1.6(R-i') + 1.9\ \ (BRi - \mathrm{LBGs}), \tag{1}$$

$$V-i' > 1.2,\ i'-z' < 0.7,\ V-i' > 1.8(i'-z') + 1.7,\ B > 28.8\ \ (Viz - \mathrm{LBGs}), \tag{2}$$

$$R-i' > 1.2,\ i'-z' < 0.7,\ R-i' > 1.0(i'-z') + 1.0,\ B > 28.8,\ V > 27.8\ \ (Riz - \mathrm{LBGs}), \tag{3}$$

$$i'-z' > 2.0,\ B > 28.8,\ V > 27.8,\ R > 28.1\ (i - \mathrm{dropouts}), \tag{4}$$

$$(B+R)/2 - NB503 > 1.2\ (NB503 - \mathrm{LAEs}), \tag{5}$$

$$(B+R)/2 - NB570 > 1.0,\ B-R > 0.5\ (NB570 - \mathrm{LAEs}), \tag{6}$$

$$i' - NB816 > 1.0,\ R-i' > 0.7\ (NB816 - \mathrm{LAEs}), \tag{7}$$

following [17, 20] and Ouchi et al. in prep. We identify about 20,000 LBGs and 1,000 LAEs from our data with these criteria. For each galaxy sample, the number of objects and the magnitude limits are summarized in Table I. BRi-LBGs, Viz-LBGs, and Riz-LBGs are located at $z = 4.0 \pm 0.5$, $z = 4.7 \pm 0.5$, and $z = 4.9 \pm 0.3$, respectively, as shown in [20], while i'-dropouts are at $z \simeq 5.9 \pm 0.3$ [22]. The redshift-distribution of LAEs is determined with the central wavelengths and FWHMs of the narrow-band filters which pass a redshifted Lyα emission line.

We carried out spectroscopic follow-up observations for these galaxies with Subaru/FOCAS [23] and VLT/VIMOS. Although it is quite difficult to obtain spectra for all the galaxies, we took spectra for part of galaxies selected from each sample. So far, we have identified about 20 LBGs and 26 LAEs, respectively. Our spectroscopic results will be summarized in Akiyama et al. in prep. The contamination rates of these galaxy samples are estimated to be $10-30\%$. Most of contaminants are foreground galaxies at $z \simeq 1$. We show spectra of securely identified eight $NB816$-LAEs in Figure 1, together with those of foreground contaminants [17].

We show the sky distribution of BRi-LBGs at $z = 4.0 \pm 0.5$ and $NB816$-LAEs at $z = 5.7 \pm 0.05$ in Figures 2 and 3 for examples of our LBG and LAE samples.

3. Results and Discussion

3.1. Angular Correlation Functions of Lyman Break Galaxies

3.1.1. Definitive Detection of Excess of Small-Scale Clustering for BRi-LBGs

We investigate BRi-LBGs detected in our data with a visual inspection, and find that a number of LBGs have close-companion LBGs. We have found 1385 pairs of BRi-LBGs with the angular distance of $2'' - 5''$, corresponding to 14-35 kpc in physical units at $z = 4$, which is beyond scales of internal structures of galaxies ($\lesssim 10$ kpc). In order to quantitatively measure the small-scale as well as large-scale clustering of LBGs, we derive the ACF $\omega(\theta)$. According to [24], the ACF is calculated by:

$$\omega(\theta) = [DD(\theta) - 2DR(\theta) + RR(\theta)]/RR(\theta), \tag{8}$$

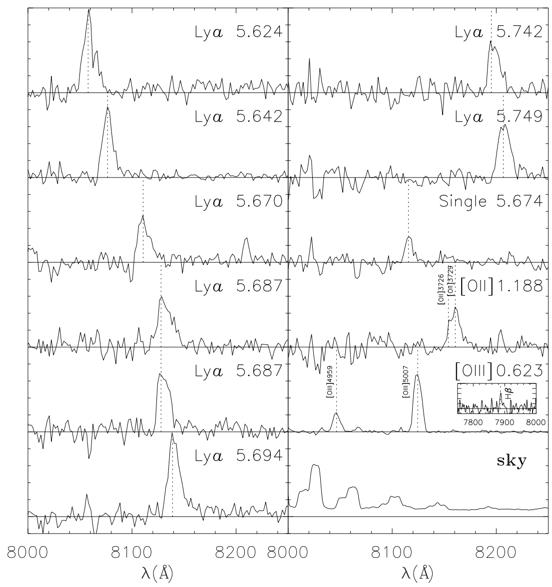

Figure 1: Spectra of eight securely identified $NB816$-LAEs, together with an unresolved-single line emitter and [OII] and [OIII] emitters. The caption on each panel indicates the classification and redshift. Ticks on the vertical axis denote 3×10^{-19} ergs s^{-1} cm^{-2} Å^{-1}, except for the following two panels because of display purpose. The second-top left and the fifth-top right panels have ticks of 6×10^{-19} and 1.5×10^{-18} ergs s^{-1} cm^{-2} Å^{-1}, respectively. The relative intensity of the night-sky emission is shown on the bottom right.

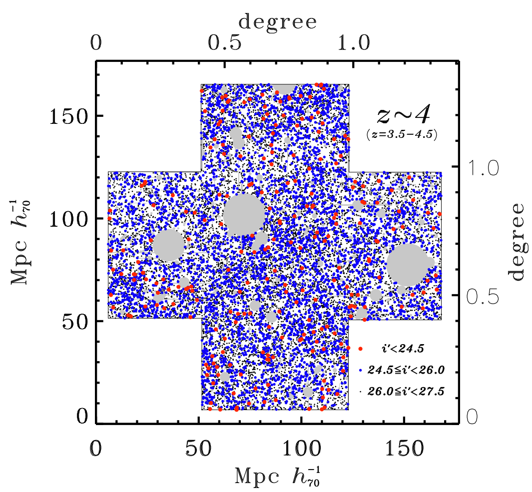

Figure 2: The distribution of BRi-LBGs at $z = 4.0 \pm 0.5$ in the SXDF. The red, blue, and black points denote the positions of the LBGs with $i' < 24.5$ (bright), $24.5 \leq i' < 26.0$ (intermediate), and $26.0 \leq i' < 27.5$ (faint), respectively. The gray areas present regions contaminated with bright stars and CCD blooming where we did not use for our analysis. The scale on the map is marked in both degrees and (comoving) megaparsecs.

where $DD(\theta)$, $DR(\theta)$, and $RR(\theta)$ are numbers of galaxy-galaxy, galaxy-random, and random-random pairs normalized by the total number of pairs in each of the three samples. We create the random sample composed of 100,000 sources with the same geometrical constraints as of the data sample. We estimate bootstrap errors for $\omega(\theta)$ [25]. The top panel of Figure 4 shows the ACF of BRi-LBGs at $z = 4.0 \pm 0.5$, together with that of dark-matter, $\omega_{\rm dm}(\theta)$ predicted by the non-linear model of [26] (see [27] for more de-

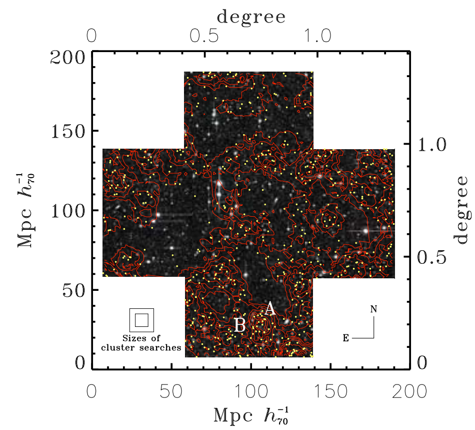

Figure 3: The distribution of $z = 5.7 \pm 0.05$ $NB816$-LAEs in the SXDF. The positions of LAEs are shown with yellow dots. The red lines correspond to contours of galaxy overdensity from $\delta_\Sigma = -0.25$ to 3.25 with a step of $\Delta = 0.50$. The characters, A and B, denote the positions of the two dense regions. The scale on the map is marked in both degrees and (comoving) megaparsecs. The large and small squares in the bottom left corner show the sizes of the surveyed areas in the previous proto-cluster searches by [9] and [10], respectively.

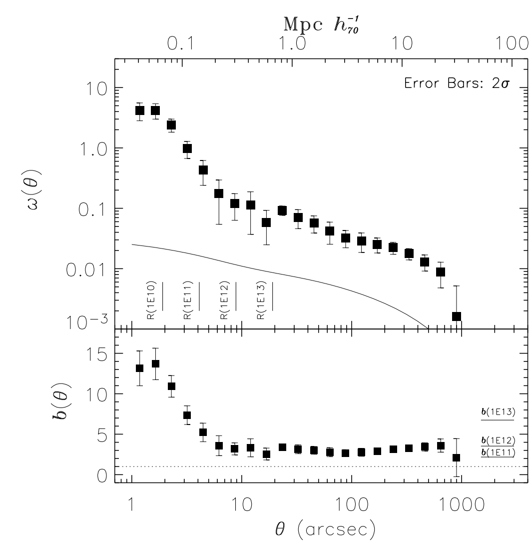

Figure 4: *Top* : The ACF, $\omega(\theta)$, of BRi-LBGs at $z = 4$. The squares and error bars indicate the ACF and bootstrap 2σ errors of BRi-LBGs. The solid curve is the ACF of dark matter predicted by the non-linear model of [26]. The scale on the top axis denotes the projected distance in comoving megaparsecs at $z = 4.0$. The ticks with R(1E10), R(1E11), R(1E12), and (1E13) correspond to the predicted virial radii of dark halos with a mass of $1 \times 10^{10} h_{70}^{-1} M_\odot$, $1 \times 10^{11} h_{70}^{-1} M_\odot$, $1 \times 10^{12} h_{70}^{-1} M_\odot$, and $1 \times 10^{13} h_{70}^{-1} M_\odot$, respectively, within which the mean enclosed density is 200 times the mean cosmic value (see [7]). *Bottom* : The galaxy-dark matter bias, b, of BRi-LBGs as a function of angular distance. The squares and error bars indicate biases and 2σ errors. The ticks with b(1E11), b(1E12), and b(1E13) show biases of dark halos with a mass of $1 \times 10^{11} h_{70}^{-1} M_\odot$, $1 \times 10^{12} h_{70}^{-1} M_\odot$, and $1 \times 10^{13} h_{70}^{-1} M_\odot$, respectively, predicted by the analytic CDM model of [6].

tails). The bottom panel of Figure 4 displays galaxy-dark matter bias as a function of angular distance in arcsecond. The bias, $b(\theta)$, is defined as

$$b(\theta) \equiv \sqrt{\omega(\theta)/\omega_{\rm dm}(\theta)}. \tag{9}$$

Since our ACF is calculated from 16,920 BRi-LBGs whose number is one-order of magnitude larger than that of the previous LBG sample (c.f. [2]), measurements in Figure 4 have unprecedentedly high signal-to-noise ratios. In Figure 4 the ACF of BRi-LBGs shows a significant excess of small scale clustering, and indicates that a single power-low function, such

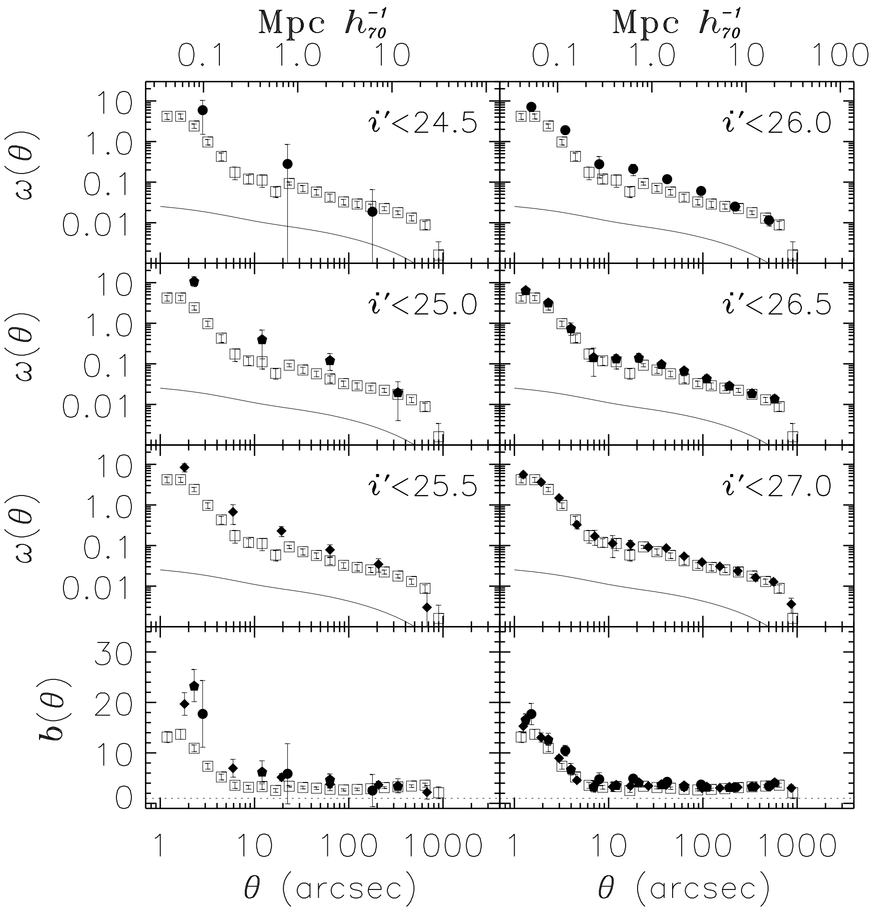

Figure 5: Magnitude dependence of the ACFs of BRi-LBGs at $z = 4.0$. In the top to third-top panels, the filled symbols are the ACFs of BRi-LBGs with the limiting magnitude indicated in the panels. Each of these panels shows the ACF of $i' < 27.5$ BRi-LBGs with the open squares. In the bottom panels, biases of LBGs for the each magnitude limit are presented with the filled symbols which correspond to those marks found in the top to third-top panels. The open squares are biases of the BRi-LBGs with $i' < 27.5$. The error bars indicate 1σ bootstrap errors in all the panels.

as $A_\omega \theta^{-\beta}$ with two free parameters of A_ω and β, does not represent the shape of the ACF in the range of $1'' - 1000''$. Comparing this ACF with the one of dark matter, we find that the small-scale excess extends up to $5'' - 8''$, i.e. $0.2 - 0.3$ comoving Mpc, which is comparable to the virial radii of dark halos with a mass of $10^{11} - 10^{12} M_\odot$. Interestingly, the large-scale average bias at $2 - 20 h_{70}$ Mpc ($60'' \lesssim \theta \lesssim 600''$) is estimated to be $\simeq 3.0 \pm 0.05$ which is also comparable to the biases of dark halos ($b = 2.2 - 3.5$) with a mass of $10^{11} - 10^{12} M_\odot$ predicted with the analytic model of the CDM [6]. This coincidence of the dark-halo mass strongly supports that $z = 4$ LBGs reside in dark halos with a mass of $10^{11} - 10^{12} M_\odot$. Moreover, these pieces of information suggest the hypothesis that multiple LBGs occupy a single dark halo (e.g. [27, 28]). The bias in small-scale at $\theta < 2''$ is $b \gtrsim 10$ which is more than three times higher than the large-scale bias. This high small-scale bias of LBGs may imply that galaxy formation is very efficient in dark halos at high redshifts.

3.1.2. Magnitude Dependence of Angular Correlation Functions for BRi-LBGs

We made six subsamples of BRi-LBGs with the limiting magnitudes of $i' < 24.5$, 25.0, 25.5, 26.0, 26.5, and 27.0. The ACFs and biases for these subsamples are derived, and presented in Figure 5, together with the ACF for all BRi-LBGs (with $i' < 27.5$). Figure 5 displays that the ACF depends on magnitude, and that a bright subsample shows a stronger ACF and a higher bias than faint subsamples. Both the small- ($\lesssim 5''$) and large- ($60'' \lesssim \theta \lesssim 600''$) scale biases monotonically decrease from $i' < 24.5$ to $i' < 27.5$. Especially, the small-scale bias shows stronger dependence on magnitude ($b \simeq 10 - 20$) than the large-scale bias ($b \simeq 3 - 4$). Comparing the bright samples of $i' < 24.5$, 25.0, and 25.5 (the top to the third-top left panels in Figure 5) with the faint sample of $i' < 27.5$, we find that the small-scale bias of bright samples is about twice higher at $\theta \sim 2'' - 3''$ than that of the faint sample, and that the outskirts of small-scale excess extend to $\theta \sim 10''$. Moreover, the large-scale

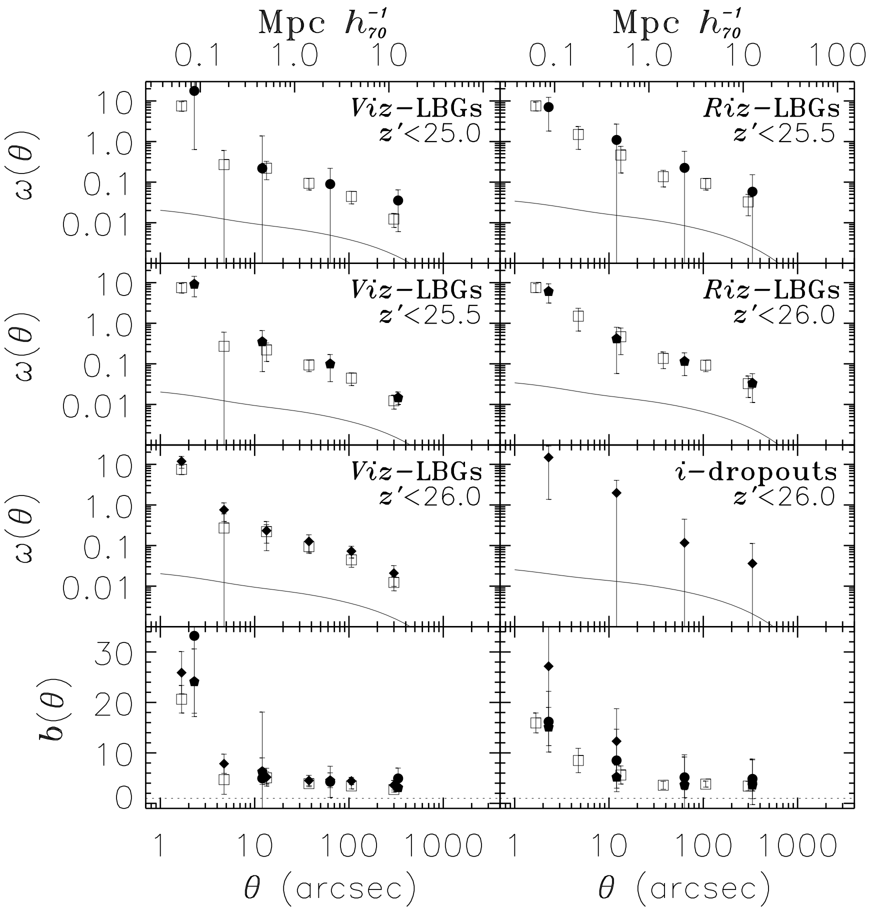

Figure 6: The ACFs of Viz-LBGs at $z = 4.7 \pm 0.5$, Riz-LBGs at $z = 4.9 \pm 0.3$, and i-dropouts at $z = 5.9 \pm 0.3$. *Left panels* : The top to third-top panels show the ACFs of Viz-LBGs with the limiting magnitudes of $z' < 25.0$, 25.5, and 26.0 (filled symbols), together with that of $z' < 26.5$ (open squares). The solid line denotes the ACF of dark-matter distribution predicted by [26]. The bottom panel is the galaxy-dark matter bias as a function of angular distance. We use the same filled symbols for the bottom panel as those displayed in the top to third-top panels. *Right panels* : Same as the left panels but for Riz-LBGs with $z' < 25.5$ (top) and 26.0 (second top) and i-dropouts with $z' < 26.0$ (third top). The open squares indicate those for Riz-LBGs with $z' < 26.5$. The error bars indicate 1σ bootstrap errors in all the panels.

bias of the bright samples ($b \sim 4$) is also higher than that of the faint sample ($b \sim 3$), which is consistent with the previous reports in [20] (see [1] for $z = 3$ LBGs). These three features of bright LBGs suggest that bright LBGs reside in more massive dark halos than faint LBGs, since massive dark halos have a high large-scale bias as well as a more occupation number and a larger halo size than less-massive dark halos, which produces the high small-scale bias with the extended outskirts of bias.

3.1.3. Angular Correlation Functions of Viz-LBGs and Riz-LBGs at $z \simeq 5$ and i-dropouts at $z \simeq 6$

Figure 6 presents the ACFs of Viz-LBGs at $z = 4.7 \pm 0.5$, Riz-LBGs at $z = 4.9 \pm 0.3$, and i-dropouts at $z = 5.9 \pm 0.3$. There is a tendency that the bias becomes stronger at higher redshifts. This tendency is found, even if we compare biases of BRi-LBGs ($z = 4$) with the other LBGs and i-dropouts ($z = 5 - 6$) for the same absolute magnitude. (Note that the absolute magnitudes become brighter for $z = 5-6$ samples than $z = 4$ sample with the same observed magnitude, and that the difference in the absolute magnitudes are $\Delta m = 0.27, 0.34$, and 0.64 for Viz-LBGs, Riz-LBGs, and i-dropouts, respectively.) The strong biases of these high-z samples is especially found at small-scales, which reach about $b = 20 - 30$ at $1'' \lesssim \theta \lesssim 5''$. This tendency implies that higher-z dark halos produce galaxies more efficiently.

3.2. Primeval Large-Scale Structures at $z = 5.7$

Since LAEs are identified by their redshifted Lyα emission line passing a narrow-band filter whose FWHM is only ~ 100Å(section 2), the redshift range of identified LAEs is significantly narrower than that of LBGs. Thus the sky distribution of LAEs presents the cosmic map of high-z galaxies, which shows detailed structures with scales of a few tens of Mpc. Figure 3 is the cosmic map showing the distribution of 515 $NB816$-LAEs at $z = 5.7 \pm 0.05$ in the SXDF. The surveyed volume has a transverse dimension of 180 Mpc $\times$ 180 Mpc and a depth of $\sim$ 40 Mpc in comoving units at $z = 5.7$. This is the first cosmic map, ever obtained, covering a $>$ 100 Mpc square area of the Universe at any high redshifts ($z > 2$). In Figure 3, the $NB816$-LAEs have a very clumpy distribution, forming concentrations with a typical size of a few Mpc, comparable in size to the proto-cluster found by [9, 10] around a radio galaxy at $z = 4.1$. These concentrations are not isolated, but connected with one another by filamentary overdense regions. The elongated overdense region of LAEs found by [12] at $z = 4.86$ may be a segment of a descendant of such a filamentary structure. There are also found several voids of ellipsoidal shapes with sizes of 10-40 Mpc in which almost no galaxy exists. The characteristic sizes of filaments and voids seen in our map are comparable to those of the present-day Universe. Thus, this map marks the discovery of primeval LSSs at $z = 5.7$.

We quantify the large-scale clumpiness of the galaxy distribution by estimating σ_{20}, the rms fluctuation of galaxy overdensity within a sphere of 20 Mpc (comoving) radius. Considering that the radial depth of the surveyed volume is about 40 Mpc, we estimate the fluctuation by $\sigma_{20}^2 \simeq \sigma_{\Sigma 20}^2 = [\langle(\Sigma_{20} - \bar{\Sigma}_{20})^2\rangle - \bar{\Sigma}_{20}]/\bar{\Sigma}_{20}^2$, where $\sigma_{\Sigma 20}$ is the rms surface overdensity within circles of 20 Mpc radius, and Σ_{20} and $\bar{\Sigma}_{20}$ are the observed number and the mean number of LAEs in a circle [29]. We obtain $\sigma_{20} = 0.4 \pm 0.2$. This σ_{20} is comparable to or at least a half the value for the present-day LSSs, i.e. $\sigma_{20}(z = 0) = 0.5 - 0.6$, obtained from galaxies with $b_j \leq 17.5$ [30]. The characteristic shapes and the rms fluctuations indicate that these primeval LSSs at $z \sim 6$ are similar to the present-day LSSs. We will present results of more detailed analyses for these primeval LSSs, such as counts-in-cell, in our forthcoming paper.

3.3. Two Clumps Identified by Spectroscopy: Forming Clusters?

We find that among the dense concentrations seen in Figure 3, the one at $2^h17^m47.2^s$, $-5°28'40''$[J2000] has the highest density contrast, $\delta_\Sigma = 3.3$, with the 4.8σ significance level, where δ_Σ is the surface overdensity for a circle of 8 Mpc radius. We refer to this concentration as Region A. Region B, a neighboring concentration at $2^h18^m19.6^s$,$-5°32'52''$[J2000], also has a high density contrast of $\delta_\Sigma = 1.5$ (2.2σ). In order to obtain three-dimensional distributions of $NB816$-LAEs in Regions A and B, we carried out spectroscopy for $NB816$-LAEs and obtained 19 LAEs with spectroscopic redshifts which includes LAEs out of Regions A and B (see [17]).

We plot in Figure 7 the three-dimensional distribution of $NB816$-LAEs for Regions A and B. The histogram of Figure 7 shows that these regions have two clumps made of 10 LAEs with a significant excess. Each of the clumps has a diameter of about 1 Mpc in physical units (7 Mpc in comoving units). For these clumps, the 1-dimensional velocity dispersion of galaxies is fairly small, $\sim$ 180 km s^{-1} (Clump A) and $\sim$ 150 km s^{-1} (B). Although these clumps may not be collapsed, the formal virial masses can be calculated from velocity dispersion, σ_{v1}, and radius, r, with $3\sigma_{v1}^2 r/G$, where G is the gravitational constant. We obtain $\sim 1 \times 10^{13} M_\odot$ (Clump A) and $\sim 8 \times 10^{12} M_\odot$ (B). The three-dimensional density contrast of $NB816$-LAEs, $\delta_n = \delta n/\bar{n}$, for the average of these clumps is ~ 80, which is comparable to those of present-day clusters, $100 - 200$. These clumps have the highest density in our surveyed volume of 9×10^5 Mpc^3 in comoving units. In the present-day Universe, this volume typically contains two massive clusters with mass of $1 - 3 \times 10^{14} M_\odot$ [31]. Thus, the discovered clumps are likely proto-clusters which are ancestors of today's such clusters.

A particularly interesting feature is that these clumps are very high concentrations of star-forming galaxies with a star-formation rate of $1 - 20 M_\odot$ yr^{-1}. The star-formation rate density (SFRD) in these clumps inferred from Lyα fluxes is about 130 times higher than in the mean of the whole 1 deg^2 field, mainly due to a large overdensity, $\delta_n \sim 80$, of $NB816$-LAEs. This very high SFRD implies that these clumps would be just producing a number of galaxies in a short period by a burst of galaxy formation. In contrast, present-day massive clusters are dominated by old early-type galaxies, and show a deficit of young star-forming galaxies [32, 33]. Since the formation epochs of early-type galaxies are estimated to be $z = 2 - 5$ or earlier (e.g. [34]), galaxies residing in these clumps are likely progenitors of the old early types seen in the core of present-day clusters. Therefore, we are probably witnessing forming clusters where a number of present-day early-type galaxies are just emerging as star-forming galaxies by a burst of galaxy formation.

3.4. Implications for Galaxy Formation

The Cold Dark Matter (CDM) model, the standard hierarchical scenario, predicts that very small initial fluctuations of mass density grow up gradually with time to evolve into galaxies and LSSs. However, the observed distribution of $NB816$-LAEs appears much more inhomogeneous than the dark-matter distribution, since the amplitude of the matter fluctuations

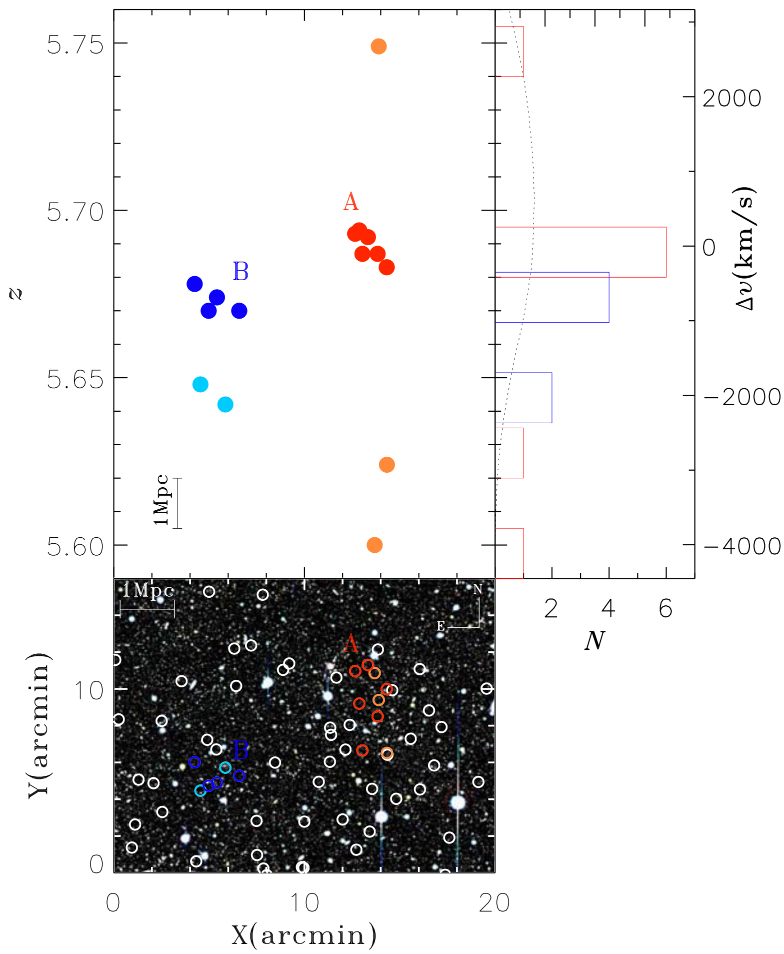

Figure 7: Three dimensional distribution of Regions A and B. The upper left panel shows the distribution of $NB816$-LAEs in transverse (East to the West) vs. radial (redshift) directions, while the bottom panel represents the distribution of $NB816$-LAEs projected on the sky. The red and blue circles correspond to the LAEs associated with the forming clusters (Clumps A and B), respectively, while the orange and cyan circles denote other LAEs in these regions. The white open circles plotted on the bottom panel denote the positions of LAEs without spectroscopic redshift. The vertical and horizontal bars indicate the length of 1 Mpc in physical units. The upper right panel shows the redshift distribution of LAEs with spectroscopic redshifts. The red and blue histograms correspond to LAEs in Regions A and B, respectively. The dotted line indicates the mean-expected number of LAEs for each region.

at $z = 5.7$ is predicted to be only 1/5 of the current value. If one wants to accept the CDM model, a solution to this discrepancy is to assume that LAEs are biased tracers of mass in a way to enhance the mass fluctuations. Previous observational studies of high-z galaxies discuss the clustering bias [1–3, 5, 35]. Theoretically, such biasing can be produced, if galaxies are formed at rare, highest peaks of yet small fluctuations of matter density (e.g. [7]). From σ_{20}, we estimate that the bias parameter, b, the ratio of galaxy overdensity to matter overdensity, is $b = 3.4 \pm 1.8$ on scales of LSSs (20 Mpc), which is comparable to the prediction at $z \sim 5$ from simulations of galaxy formation based on the CDM model [36, 37]. Thus, the CDM model may be consistent with the early formation of LSSs that we discovered, though the model needs to reproduce the characteristic shapes of observed LSSs, long filaments and large voids. On the other hand, we estimate the b value, in the CDM, which reproduces the observed number of forming clusters (two in 9×10^5 Mpc^3) with the size and the overdensity, $\delta_n \sim 80$, following the prescription of [12, 38]. Although this estimation of b is based on small statistics and might include a large error due to cosmic variance, we obtain $b \sim 30$ for the two forming clusters, which is about ten times higher than the value for LSS scales,. This variety of b could be due to the dependence of b on the clustering scale or galaxy density [39]. In fact, section 3.1.3 shows that small-scale biases of $z \simeq 5$ LBGs reach $b = 20 - 30$ at $1'' \lesssim \theta \lesssim 5''$. We note that the angular scale of such a large bias is very small ($\lesssim 0.2$ comoving Mpc in projection). However, it would be possible that these forming clusters are made of a massive dark halo with a larger outskirt of an actively galaxy-forming region than those of field LBGs. These very high bias may be also explained by a burst of galaxy formation that very efficient galaxy formation takes place in a dark halo at these high redshifts.

Acknowledgments

We are grateful to the Subaru Telescope staff for their help to obtain these precious data sets. M. Ouchi has been supported by the Hubble Fellowship program through grant HF-01176.01-A awarded by the Space Telescope Science Institute, which is operated by the Association of Universities for Research in Astronomy, Inc. under NASA contract NAS 5-26555.

References

[1] Giavalisco, M. & Dickinson, M. 2001, ApJ, 550, 177
[2] Ouchi, M. et al. 2001, ApJ, 558, L83
[3] Ouchi, M., et al. 2004b, ApJ, 611, 685
[4] Ouchi, M. et al. 2003, ApJ, 582, 60
[5] Shimasaku, K., et al. 2004, ApJ, 605, L93
[6] Sheth, R. K., & Tormen, G. 1999, MNRAS, 308, 119
[7] Mo, H. J. & White, S. D. M. 2002, MNRAS, 336, 112
[8] Steidel, C. C., Adelberger, K. L., Dickinson, M., Giavalisco, M., Pettini, M., & Kellogg, M. 1998, ApJ, 492, 428
[9] Venemans, B. P. et al. 2002, ApJ, 569, L11
[10] Miley, G. K., et al. 2004, Nature, 427, 47
[11] Venemans, B. P., et al. 2004, A&A, 424, L17
[12] Shimasaku, K. et al. 2003, ApJ, 586, L111
[13] Ajiki, M., et al. 2003, AJ, 126, 2091
[14] Hu, E. M., Cowie, L. L., Capak, P., McMahon, R. G., Hayashino, T., & Komiyama, Y. 2004, AJ, 127, 563
[15] Sekiguchi, K. et al. 2004, Astrophysics and Space Science Library, 301, 169
[16] Miyazaki, S. et al. 2002, PASJ, 54, 833
[17] Ouchi, M., et al. 2005, ApJ, 620, L1
[18] Rhoads, J. E., et al. 2003, AJ, 125, 1006
[19] Yagi, M., Kashikawa, N., Sekiguchi, M., Doi, M., Yasuda, N., Shimasaku, K., & Okamura, S. 2002, AJ, 123, 66
[20] Ouchi, M., et al. 2004a, ApJ, 611, 660
[21] Bertin, E. & Arnouts, S. 1996, A&AS, 117, 393
[22] Shimasaku, K., et al. Submitted to PASJ
[23] Kashikawa, N. et al. 2002, PASJ, 54, 819
[24] Landy, S. D., & Szalay, A. S. 1993, ApJ, 412, 64
[25] Ling, E. N., Barrow, J. D., & Frenk, C. S. 1986, MNRAS, 223, 21P
[26] Peacock, J. A., & Dodds, S. J. 1996, MNRAS, 280, L19
[27] Hamana, T., Ouchi, M., Shimasaku, K., Kayo, I., & Suto, Y. 2004, MNRAS, 347, 813
[28] Cooray, A., & Sheth, R. 2002, Phys. Rep., 372, 1
[29] Peebles, P. J. E. 1980, The Large-Scale Structure of the Universe (Princeton: Princeton Univ. Press)
[30] Seaborne, M. D., et al. 1999, MNRAS, 309, 89
[31] Reiprich, T. H. & Böhringer, H. 2002, ApJ, 567, 716
[32] Dressler, A. 1980, ApJ, 236, 351
[33] Butcher, H. & Oemler, A. 1984, ApJ, 285, 426
[34] Kodama, T., Arimoto, N., Barger, A. J., & Arag'on-Salamanca, A. 1998, A&A, 334, 99
[35] Adelberger, K. L., Steidel, C. C., Giavalisco, M., Dickinson, M., Pettini, M., & Kellogg, M. 1998, ApJ, 505, 18
[36] Baugh, C. M., Benson, A. J., Cole, S., Frenk, C. S., & Lacey, C. G. 1999, MNRAS, 305, L21
[37] Kauffmann, G., Colberg, J. M., Diaferio, A., & White, S. D. M. 1999, MNRAS, 307, 529
[38] Steidel, C. C., Adelberger, K. L., Shapley, A. E., Pettini, M., Dickinson, M., & Giavalisco, M. 2000, ApJ, 532, 170
[39] Benson, A. J., Frenk, C. S., Baugh, C. M., Cole, S., & Lacey, C. G. 2001, MNRAS, 327, 1041